Integrated InP-InGaAsP tunable coupled ring optical bandpass filters with zero insertion loss

Robert S. Guzzon,* Erik J. Norberg, John S. Parker, Leif A. Johansson, and Larry A. Coldren

Department of Electrical and Computer Engineering, University of California Santa Barbara, Santa Barbara, California 93116, USA
*guzzon@ece.ucsb.edu

Abstract: Second and third-order monolithically integrated coupled ring bandpass filters are demonstrated in the InP-InGaAsP material system with active semiconductor optical amplifiers (SOAs) and current injection phase modulators (PMs). Such integration achieves a high level of tunability and precise generation of optical filters in the RF domain at telecom wavelengths while simultaneously compensating for device insertion loss. Passband bandwidth tunability of 3.9 GHz to 7.1 GHz and stopband extinction up to 40 dB are shown for third-order filters. Center frequency tunability over a full free spectral range (FSR) is demonstrated, allowing for the placement of a filter anywhere in the telecom C-band. A Z-transform representation of coupled resonator filters is derived and compared with experimental results. A theoretical description of filter tunability is presented.

©2011 Optical Society of America

OCIS codes: (250.5300) Photonic integrated circuits; (230.5750) Resonators; (350.2460) Filters, interference; (130.7408) Wavelength filtering devices.

References and links

1. C. K. Madsen and J. H. Zhao, *Optical Filter Design and Analysis: A Signal Processing Approach* (Whiley-Interscience, 1999), Chap. 1.
2. J. Capmany, B. Ortega, and D. Pastor, "A tutorial on microwave photonic filters," J. Lightwave Technol. **24**(1), 201–229 (2006).
3. P. Dong, N. N. Feng, D. Feng, W. Qian, H. Liang, D. C. Lee, B. J. Luff, T. Banwell, A. Agarwal, P. Toliver, R. Menendez, T. K. Woodward, and M. Asghari, "GHz-bandwidth optical filters based on high-order silicon ring resonators," Opt. Express **18**(23), 23784–23789 (2010).
4. N. N. Feng, P. Dong, D. Feng, W. Qian, H. Liang, D. C. Lee, J. B. Luff, A. Agarwal, T. Banwell, R. Menendez, P. Toliver, T. K. Woodward, and M. Asghari, "Thermally-efficient reconfigurable narrowband RF-photonic filter," Opt. Express **18**(24), 24648–24653 (2010).
5. M. Rasras, K. Tu, D. Gill, Y. Chen, A. White, S. Patel, A. Pomerene, D. Carothers, J. Beattie, M. Beals, J. Michel, and L. Kimerling, "Demonstration of a tunable microwave-photonic notch filter using low-loss silicon ring resonators," J. Lightwave Technol. **27**(12), 2105–2110 (2009).
6. B. E. Little, S. T. Chu, P. P. Absil, J. V. Hryniewicz, F. G. Johnson, F. Seiferth, D. Gill, V. Van, O. King, and M. Trakalo, "Very high-order microring resonator filters for WDM applications," IEEE Photon. Technol. Lett. **16**(10), 2263–2265 (2004).
7. M. S. Dahlem, C. W. Holzwarth, A. Khilo, F. X. Kärtner, H. I. Smith, and E. P. Ippen, "Reconfigurable multi-channel second-order silicon microring-resonator filterbanks for on-chip WDM systems," Opt. Express **19**(1), 306–316 (2011).
8. J. Park, T. Lee, D. Lee, S. Kim, W. Hwang, and Y. Chung, "Widely tunable coupled-ring-reflector filter based on planar polymer waveguide," IEEE Photon. Technol. Lett. **20**(12), 988–990 (2008).
9. H.-W. Chen, A. W. Fang, J. D. Peters, Z. Wang, J. Bovington, D. Liang, and J. E. Bowers, "Integrated microwave photonic filter on a hybrid silicon platform," IEEE Trans. Microw. Theory Tech. **58**(11), 3213–3219 (2010).
10. R. S. Guzzon, E. J. Norberg, J. S. Parker, L. A. Johansson, and L. A. Coldren, "Monolithically integrated programmable photonic microwave filter with tunable inter-ring coupling," *Proc. IEEE Conf. Microwave Photonics* (IEEE, Montreal, Canada, 2010).
11. D. M. Baney, P. Gallion, and R. S. Tucker, "Theory and measurement techniques for the noise figure of optical amplifiers," Opt. Fiber Technol. **6**(2), 122–154 (2000).
12. C. K. Madsen and J. H. Zhao, *Optical Filter Design and Analysis: A Signal Processing Approach* (Whiley-Interscience, 1999), Chap. 3.

13. S. Darmawan, Y. M. Landobasa, and M.-K. Chin, "Pole-zero dynamics of high-order ring resonator filters," J. Lightwave Technol. **25**(6), 1568–1575 (2007).
14. J. Simon, P. Doussiere, P. Lamouler, I. Valiente, and R. Riou, "Travelling wave semiconductor optical amplifier with reduced nonlinear distortions," Electron. Lett. **30**(1), 49–50 (1994).
15. P. Saeung and P. P. Yupapin, "Generalized analysis of multiple ring resonator filters: modeling by using graphical approach," Optik (Stuttg.) **119**(10), 465–472 (2008).
16. R. S. Guzzon, E. J. Norberg, J. S. Parker, and L. A. Coldren, "Highly programmable optical filters integrated in InP-InGaAsP with tunable inter-ring coupling," *Conf. Integrated Photonics Research, Silicon and Nanophotonics* (Optical Society of America, Monterey, CA, 2010).
17. J. W. Raring, M. N. Sysak, A. T. Pedretti, M. Dummer, E. J. Skogen, J. S. Barton, S. P. Denbaars, and L. A. Coldren, "Advanced integration schemes for high-functionality/high-performance photonic integrated circuits," Proc. SPIE **6126**, 61260H, 61260H-20 (2006).
18. T. Darcie, R. Jopson, and R. Tkach, "Intermodulation distortion in optical amplifiers from carrier-density modulation," Electron. Lett. **23**(25), 1392–1394 (1987).
19. E. Norberg, R. Guzzon, and L. Coldren, "Programmable photonic filters fabricated with deeply etched waveguides," in *Proc. of IEEE Conf. on Indium Phosphide and Related Materials* (IEEE Photonics Society, Newport beach, CA, 2009), pp. 163–166.
20. G. P. Agrawal, *Fiber-Optic Communication Systems* (Whiley-Interscience, 2002), Chap. 6.
21. J. S. Parker, E. J. Norberg, R. S. Guzzon, S. C. Nicholes, and L. A. Coldren, "High verticality InP/InGaAsP etching in $Cl_2/H_2/Ar$ inductively coupled plasma for photonic integrated circuits," J. Vac. Sci. Technol. B **29**(1), 011016 (2011).

1. Introduction

Filtering in the optical domain can be useful for many systems in which data is modulated on an optical carrier. In the telecom world, applications can be found in WDM channel add-drop filters and gain flattening filters [1]. For analog signal processing at RF frequencies, microwave photonic filters can have advantages over all-electronic systems due to their wide tunability, programmability, and immunity to electromagnetic interference. For example, radio-over-fiber (RoF) systems that employ an array of remote antennas benefit from the low loss transmission properties of optical fiber, thus opening up the possibility of pre-filtering in the optical domain before analog-to-digital conversion. In particular, radar systems can benefit from the ultra-wide bandwidth of a tunable optical filter in channelizing and matched filter applications [2].

System performance depends greatly on the accuracy with which optical filter responses are synthesized. For example, an ideal bandpass filter has a flat passband, high extinction, fast roll-off, and is linear-time-invariant (LTI). Optical fiber and bulk optical component based photonic filters suffer from thermal and mechanical instability, and are therefore limited mostly to the incoherent regime, which has significant performance drawbacks [2]. Size, weight, power, and cost are also an issue with bulk optical systems. Monolithic integration offers a stable, compact scheme for construction of filter geometries, and recently many filters have been demonstrated in various integration platforms to realize both telecom and microwave photonic filters [3–10]. Integration in passive systems (those without optical gain) relies on low loss waveguides to maintain filter shape and minimize insertion loss. Silicon photonics and polymer waveguide photonics are two such solutions [3–8]. However, generating optimal filter shapes in such systems depends strongly on setting waveguide coupling values accurately and creating extremely low loss waveguides. Furthermore, these systems are ultimately limited in complexity by accrued loss, which degrades the system dynamic range [11]. Active systems, utilizing direct-bandgap semiconductors with gain at telecom wavelengths have been shown in a variety of material systems including InP/InGaAsP and hybrid SOI/InP [9,10]. The optical gain provided in these integration platforms can account for accumulated losses and more easily synthesize optimal filter shapes by adding a degree of amplitude tunability unavailable in passive systems. However, degradation of dynamic range from amplified spontaneous emission (ASE) noise and non-linear saturation of gain in semiconductor optical amplifiers (SOAs) is a concern that must be addressed [11].

Filters can be constructed of infinite impulse response (IIR) and/or finite impulse response (FIR) elements. Filters with IIR elements are better able to synthesize high-quality bandpass filters using fewer stages [12], and are the focus of this effort. IIR filters constructed out of

integrated waveguide rings can be arranged in one of two geometries: cascaded or coupled. In a coupled system, there is optical feedback from each ring to the previous ring, contrary to the cascaded geometry. Each design has advantages, but the coupled geometry can easily synthesize the complex-conjugate poles required of bandpass filters, and do so while requiring lower amplifier gain (or tolerating higher waveguide losses) than a comparable cascaded system. Previously, we have reported on 3rd order coupled-ring filter photonic integrated circuit (PIC) and published preliminary results [10]. Here we examine the system in more theoretical detail, show good agreement between theory and experiment, and demonstrate high levels of tunability while maintaining an optimal filter shape.

2. Coupled-ring optical filters and their z-transform representation

2.1 Z-transform for optical systems

The Z-transform is a convenient method for representing the transfer function of optical filters if all optical delays are assumed to be an integer multiple of some unit delay [12,13]. This discrete-time approach accurately models the set of identical filter responses each separated in frequency by a free spectral range (FSR) that are obtained in an LTI optical system. In general, optical feedback from rings or Fabry-Perot cavities creates system poles, while feed-forward geometries such as a Mach-Zehnder Interferometer (MZI) create system zeros. The poles and zeros of such a system can be represented on the complex frequency plane. This pole-zero plot is a convenient tool for understanding the effect of varying device parameters on the filter shape.

An active optical system with feedback must remain below the lasing threshold in order to maintain gain tunability. Above threshold, the carrier density and gain in each SOA is clamped. While higher SOA linearity can be achieved in this regime [14], the loss of tunability is detrimental to a large system such as the one described here. From a signal processing standpoint, the pole magnitude generated across the spectrum varies due to variations in gain and loss with wavelength. Therefore, at the operating wavelength, the pole magnitude may be suboptimal in order to keep the entire system below lasing. Pole magnitudes of < 0.9 are typically achievable in practice.

There are a variety of ways to determine the scattering parameters of an optical circuit, including transfer matrix approaches, block diagram simplification, and Mason's formula for single-input single-output systems [12,15]. The equation

$$z = e^{j\omega_n} = e^{j\beta L_U} \tag{1}$$

transforms device scattering parameters to the z-domain. ω_n is the normalized frequency, L_U is the unit length, taken as the ring length in our devices, and β is the propagation constant given by

$$\beta = \frac{2\pi n_{eff}}{\lambda} \tag{2}$$

where n_{eff} is the effective index of refraction and λ is the optical wavelength.

Optical bandpass filters are generated with the fewest amount of stages using IIR-type filters [12]. Optimal Chebyshev Type I and Butterworth filters are created in the Z-domain using equal numbers of poles and zeros. However, reasonable approximations can be synthesized with pole-only filters. In the next section, we analytically compare the Z-transform representations of two types of 2nd order IIR filters.

2.2 Second-order cascaded and coupled rings

Figure 1 shows schematic representations of ring geometries that can synthesize two poles anywhere in the complex plane. Pole angles are set by phase modulators, and pole magnitudes are set by intracavity loss. The total intracavity loss is made up of waveguide propagation loss and losses from coupling out of the ring. The loss is offset by intracavity amplifier gain. In the

cascaded case, there is no optical feedback from the 2nd ring into the 1st ring, and so the pole locations and magnitudes are independently set by each ring's tuning parameters. In contrast, the poles generated by the coupled ring system are dependent on the tuning parameters from both rings. In particular, the poles from a coupled ring geometry cannot be located at the same frequency. They will split into two peaks of equal magnitude. The distance between the peaks is determined by the inter-ring coupling value.
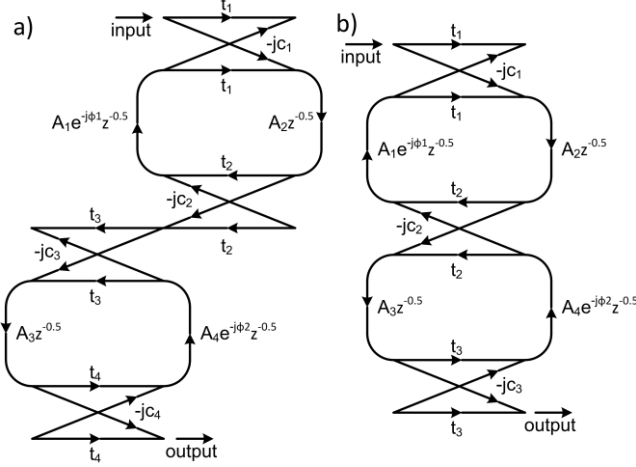
Fig. 1. Signal flow graphs of 2nd order ring filters. (a) Cascaded case with no feedback from the 2nd ring to the 1st ring. (b) Coupled case with feedback. c and t are amplitude coupling and transmission values for the couplers, the ϕ's are the added phase from phase modulators, and the A's are the multiplicative gain through a waveguide section.

Mason's formula for determining the transfer function from a signal flow graph can be used to write the scattering parameters for these two systems [15]. The amplitude transfer functions for two cascaded rings and two coupled rings are as follows

$$H_{cascaded}(z) = \frac{c_1 c_2 c_3 c_4 A_2 A_3 z^{-1}}{1 - B_1 z^{-1} + B_2 z^{-2}} \tag{3}$$

$$H_{coupled}(z) = \frac{j c_1 c_2 c_3 A_2 A_3 z^{-1}}{1 - D_1 z^{-1} + D_2 z^{-2}} \tag{4}$$

where

$$B_1 = t_1 t_2 A_1 A_2 e^{-j\varphi_1} + t_3 t_4 A_3 A_4 e^{-j\varphi_2} \tag{5}$$

$$B_2 = t_1 t_2 t_3 t_4 A_1 A_2 A_3 A_4 e^{-j(\varphi_1 + \varphi_2)} \tag{6}$$

$$D_1 = t_1 t_2 A_1 A_2 e^{-j\varphi_1} + t_2 t_3 A_3 A_4 e^{-j\varphi_2} \tag{7}$$

$$D_2 = t_1 t_3 A_1 A_2 A_3 A_4 e^{-j(\varphi_1 + \varphi_2)}. \tag{8}$$

where c_i is the amplitude coupling value of the ith coupler, and there is assumed to be no coupler insertion loss, implying $t_i = \sqrt{1 - c_i^2}$. ϕ_i is the phase introduced by the phase modulator in the ith ring, A_i is the fractional amplitude loss in each waveguide segment given by

$$A_i = e^{\frac{\Gamma g_i - \alpha_a}{2} L_{SOA}} e^{\frac{\alpha_p}{2}\left(\frac{L}{2} - L_{SOA}\right)} \tag{9}$$

where Γg_i is the modal power gain and α_a is the modal loss from the Semiconductor Optical Amplifier (SOA) in the ith waveguide segment, L_{SOA} is the length of the SOAs, α_p is the passive modal waveguide loss, and L is the ring length. Equation (3) and (4) are very similar, but result in different behavior due to the coupled nature of the z^{-1} and z^{-2} terms in the coupled ring equation.

The pole magnitudes of the cascaded system are set independently by each ring, and are equal simply to the round-trip gain minus loss. In the coupled system, the poles can be determined by finding the roots of the denominator, which can be written in terms of the intrinsic ring round-trip gain minus loss, p_r. This "intrinsic pole" is the pole obtained from the ring independent of any feedback from other rings, as in the cascaded system. These intrinsic poles are given by

$$p_{r,1} = t_1 t_2 A_1 A_2 e^{-j\varphi_1} \tag{10}$$

$$p_{r,2} = t_2 t_3 A_3 A_4 e^{-j\varphi_2} \tag{11}$$

Substituting Eq. (10) and (11) into Eq. (4) and solving for the roots of the denominator, the actual poles of the coupled system are determined to be

$$p_{coupled,\pm} = \frac{1}{2}\left(p_{r,1} + p_{r,2}\right) \pm \frac{1}{2} j \sqrt{\frac{4 p_{r,1} p_{r,2}}{1-C_2} - \left(p_{r,1} + p_{r,2}\right)^2} \tag{12}$$

where C_2 is the power coupling in coupler 2 (i.e. $C_2 = c_2^2$). If the term under the square root is real, then the poles are complex conjugates of each other. When $\phi_1 = \phi_2$, the ring resonances are located at the same frequency which is most interesting for the bandpass filter application. For this case, $p_{r,1}$ and $p_{r,2}$ are real, and the pole magnitudes are both given by

$$\left|p_{coupled,\pm}\right| = \sqrt{\frac{p_{r,1} p_{r,2}}{1-C_2}} \tag{13}$$

This situation has important implications. The first is that the magnitudes of the two poles are always equal, regardless of the individual intrinsic pole magnitudes. The second is that the pole magnitudes are enhanced above the level of the intrinsic (cascaded) pole magnitudes by a factor of $1/\sqrt{1-C_2}$. These effects make the coupled-ring geometry advantageous for easily synthesizing bandpass filters, by simply creating a symmetric response and requiring less gain than the cascaded system in order to reach the same pole magnitudes.

Taken a step further, if the intrinsic pole magnitudes are equal, the pole angles can be written from Eq. (12) simply as

$$\angle p_{coupled,\pm} = \tan^{-1} \sqrt{\frac{C_2}{1-C_2}} \tag{14}$$

The pole angle determines the bandwidth of the filter; as C2 increases, the bandwidth increases.
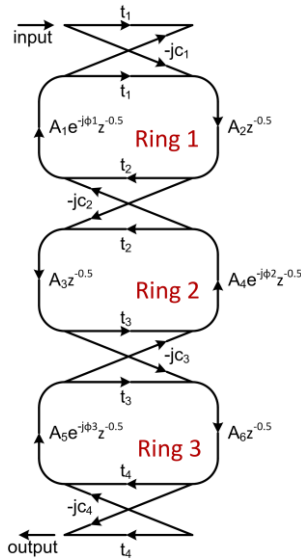
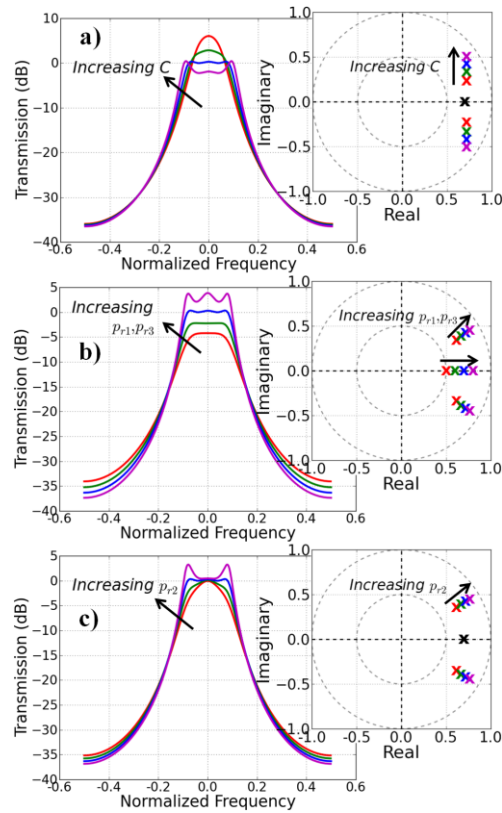Fig. 2. Signal flow graph for a 3rd order coupled ring filter.

Fig. 3. Theoretical filter shapes and pole-zero plots for a 3rd order coupled ring filters showing variation with (a) tuning inter-ring coupling, (b) tuning the intrinsic pole magnitude of the 1st and 3rd rings, and (c) tuning the intrinsic pole magnitude of the 2nd ring. In all cases, the blue filter is the same, employing an inter-ring coupling value of 0.15, and intrinsic pole magnitudes of 0.7 for rings 1 and 3, and 0.73 for ring 2.

2.3 Third-order coupled rings

The 3rd order coupled system is similar in operation to the 2nd order system. However, due to the complexity of the equations, we will present the operation here qualitatively. A signal flow graph of a 3rd order coupled system is shown in Fig. 2. Like the 2nd order system, when all three ring resonances are located at the same frequency, there is a splitting in the system poles. In this case, there is one real pole located at zero normalized frequency, and two complex conjugate poles. Similarly to the 2nd order system, the complex conjugate poles share a pole magnitude that is dependent on all three of the intrinsic ring pole magnitudes.

Figure 3 shows how the poles move in the complex plane when various tuning parameters are adjusted. When the inter-ring coupling values are increased, the complex part of the complex conjugate pair of poles is increased (Fig. 3(a)). The two coupling values, C_2 and C_3, do not need to be equal for the filter to be symmetric, and adjusting just one of them affects both complex conjugate poles.

When the intrinsic pole magnitude of the 2nd ring is increased, the center system pole does not change, but the complex conjugate poles move towards the unit circle (Fig. 3(b)). In effect, this sets the "evenness" of the three filter passband maxima. Once the evenness is set, the magnitude of the passband ripple can be varied by adjusting the intrinsic ring pole magnitudes of the 1st and 3rd rings (Fig. 3(c)). Again, similarly to the 2nd order filter, these do not need to be the same to achieve a symmetric filter. In this way, a bandpass filter with a specified passband ripple can be set over a range of bandwidths. As long as the ring resonances are located at the same frequency, a symmetric bandpass filter is synthesized, even if the intrinsic ring pole magnitudes and the inter-ring coupling values are not equal.

3. Design of the monolithically integrated filter

3.1 System design

Figure 4 shows a schematic representation of the 3rd order coupled-ring filter, termed a unit cell. The 3-ring structure can synthesize 1st order poles, 2nd order coupled poles, 2nd order cascaded poles, and 3rd order coupled poles. In addition, a 1st order zero is formed by the interference of the feed forward path and the path through the rings. The rings are 3 mm long, producing an FSR of 0.212 nm or 26.5 GHz.
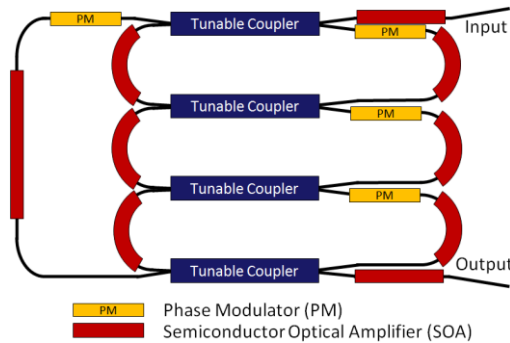

Fig. 4. Schematic representation of our proposed 3rd order coupled ring unit cell with SOAs in red, phase modulators (PMs) in yellow, and MZI tunable couplers in blue. The feed-forward waveguide on the left forms an MZI with the path through the rings.

The SOAs and phase modulators are P-i-N diodes, and are operated by forward-bias current injection. The SOAs can also be operated under reverse-bias as detectors that effectively "shut-off" waveguide paths to change the filter configuration. The tunable couplers are symmetric MZIs with a 300 μm phase modulator in each waveguide path. Splitting in the MZI is provided by 3 dB 2x2 restricted interference multi-mode-interference (MMI) couplers, each 100 μm long. By tuning the phase in one waveguide, the coupling is fully tunable. Power cross-coupling values less than −20 dB of total output power were demonstrated [16]. As the

inter-ring coupling determines the frequency splitting of coupled poles [Eq. (14)], this metric is critical for creating narrow bandwidth and high extinction ratio filters. Total tunable coupler insertion loss was measured to be < 1.5 dB. Light it coupled on and off chip via a flared and angled waveguide at the facet to lensed fiber. Flaring the waveguides adiabatically from 2.8 μm to 5.0 μm helps provide better matching to the lensed fiber mode, while a 7° angle at the facet reduces reflections.

While the unit cell is highly tunable in both frequency and bandwidth, a lower limit on bandwidth is imposed by the minimum coupling values and the maximum pole magnitudes that can be obtained. In order to create filters narrower than the 3 GHz shown in the results, longer delay lengths are needed. Extension of the unit cell to longer rings and narrower bandwidths would require appropriate SOA gain to compensate for additional waveguide loss. To create wider filters, or to enhance extinction and roll-off, multiple unit cells can be cascaded monolithically. In this way, filter transfer functions are multiplied together. The FSR of an optical filter is also crucial to its functionality. The 1st order zero is designed such that it can enhance the FSR by a factor of 2 if two unit cells are cascaded together. The FSR of the zero is twice that of the poles, and when cascaded with a unit cell synthesizing a bandpass filter, can reduce the passband level in every other filter order. This in effect would enhance the FSR by a factor of 2. Other, more elaborate designs could be envisioned where bandpass filters of different FSR (and passband bandwidths) could be cascaded to create a narrowband filter with a large FSR.

3.2 Active/passive integration and waveguide design

In order to fabricate on the same device active SOAs with gain in the telecom C-band, passive low-loss waveguides, and fast phase modulators, a multi-purpose integration scheme is needed. Many different methods of integration in InP/InGaAsP have been proposed and demonstrated in the centered quantum well (CQW) or offset quantum well (OQW) epitaxial structures [17]. Here we utilize an OQW integration platform because of its ease of fabrication and high linearity compared to CQW designs. The OQW material structure consists of quantum wells grown above the transverse waveguide layer. This offset from the center of the optical mode decreases the confinement factor with the quantum wells, decreasing the gain, increasing the saturation power, and increasing RF linearity [17,18]. Since the required gain in each SOA is very low for this application and linearity is important, the OQW structure is suitable. Advantageously, active / passive definition is relatively simple, involving a selective wet etch of the quantum wells and a single blanket regrowth to provide the p-InP cladding and p-InGaAs contact layer. The OQW platform also creates low-loss passive waveguide sections (~1 dB/mm [19]) which are crucial for developing a system with low noise Fig [20]. Due to the use of compressively strained quantum wells, the SOAs display high polarization dependence, providing much higher gain for TE than TM polarized light. This dependence would need to be addressed in the context of the final RF photonic link. More details about the material structure can be found in [17].

To provide lateral confinement of the optical mode, a deeply-etched waveguide geometry was chosen. In such a design, the lateral waveguide is defined with a deep dry etch through the transverse waveguide layer. This provides high optical confinement, allowing for tight waveguide bends with minimal radiation loss. The etch quality is important for avoiding excess optical scattering loss, and we have developed such an etch using an $H_2/Cl_2/Ar$ ICP-RIE recipe [21]. Previously, we have demonstrated low loss waveguides (~1 dB/mm) and sufficient SOA gain (26 dB/mm) for our devices using this integration platform [19]. The waveguides are 2.8 μm wide in the SOAs and taper down to 1.8 μm at the MMI couplers. While the waveguides are multi-mode, the device structure operates in a single-mode fashion due to 2nd order mode excess loss in the MMIs, estimated to be ~5 dB. The OQW material structure paired with the low loss deeply-etched waveguide is a robust and simple integration platform that, together with standard optical lithography, promises a high yield suitable for commercial volume production schemes.

3.3 Fabrication

The fabrication of the filters was performed with a simple 4 mask-layer process. After active / passive patterning and regrowth of the p-InP cladding and p-InGaAs contact layer, the waveguides were defined using standard i-line stepper lithography. In order to accurately transfer the waveguide mask to the InP, a Cr/SiO_2 hardmask was defined with photo-resist [21]. After the waveguide etch, 300 nm of protective nitride was deposited to act as an electric insulator, and to protect the etched waveguide sidewalls. Vias were then opened to the InGaAs contact layer for electrical contact to the SOAs and phase modulators. P-contacts were evaporated onto this surface while the n-contact was evaporated onto the backside of the n-conducting substrate. Figure 5 shows a mounted device and a close-up view of an MMI-coupler highlighting the smooth and anisotropic waveguide etch.
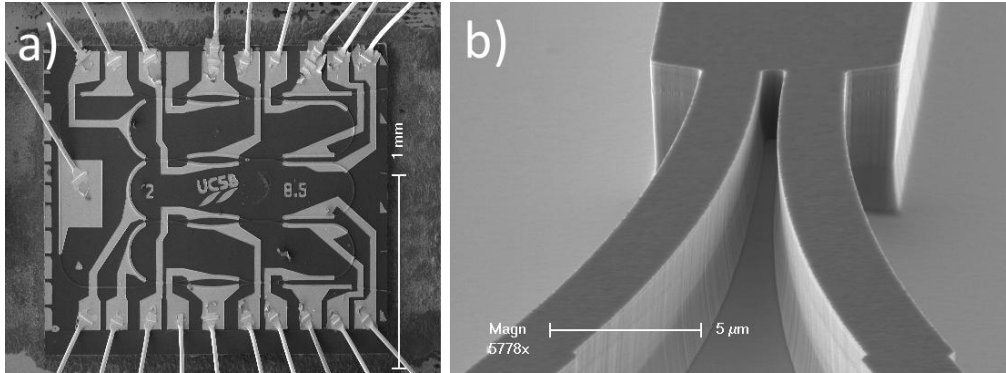

Fig. 5. Scanning electron microscope (SEM) image of (a) a fabricated, mounted, and wire-bonded unit cell; and (b) input/output waveguides of a deeply-etched MMI coupler.
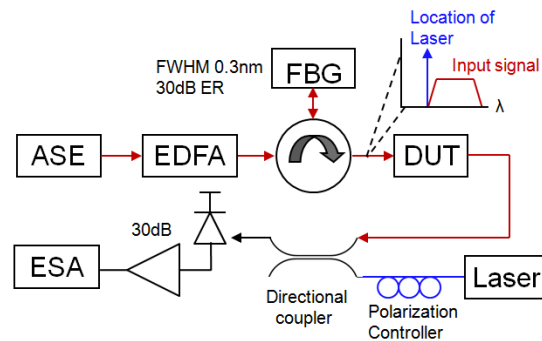

Fig. 6. Schematic of the measurement setup. A broadband ASE source is band-limited by a fiber Bragg grating (FBG) filter and then propagated through the device under test (DUT). The response is viewed on an ESA after heterodyne down conversion by a tunable laser.

4. Measured filter results

4.1 Measurement setup

The bandpass filters shown in Fig. 7 were measured at microwave frequencies by heterodyne down conversion of a filtered broadband optical signal. In order to create this broadband input, an Erbium-doped fiber ASE source was used. Figure 6 is a schematic of the measurement setup.
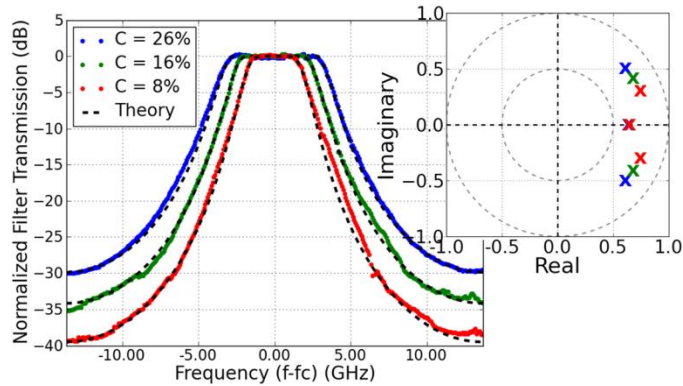
Fig. 7. Measured coupled-ring 3rd order bandpass filters with theoretical fits and their respective pole locations. The three filters are for coupling values of 25.5%, 15.6%, and 8.41%, producing bandwidths of 7.06, 5.50, and 3.90 GHz and extinction ratios of 30, 35, and 40 dB. The theoretical fits are good, indicating that the device was operating in the linear regime.
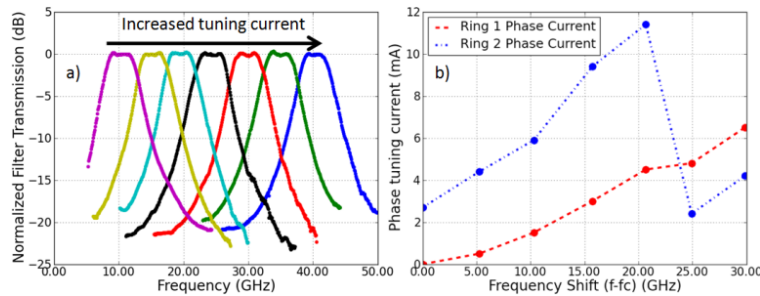

Fig. 8. (a) Measured 2nd order coupled ring filters showing tunability in frequency. The overall response is normalized to 0 dB, but the relative amplitudes of the filters are real. The unit cell itself had a throughput optical gain during this test of ~3 dB. (b) PM currents required in each of the two rings in order to tune the filter. The large shift in the ring 2 phase current at 25 GHz occurred when the next longitudinal mode (located 1 FSR away) was utilized, demonstrating the smooth tunability of filters across multiple FSRs. In this way, filters can be placed anywhere in the telecom C-band.
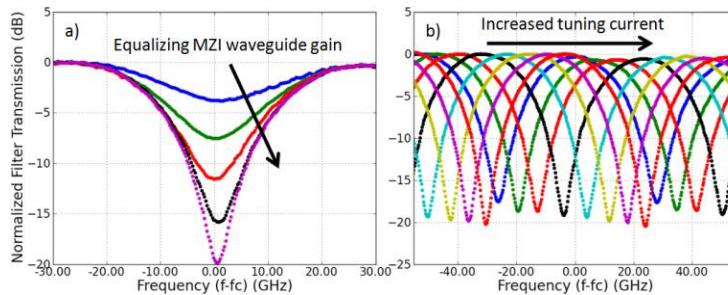

Fig. 9. Optically measured MZI zero filters. (a) Showing tunability in extinction by equalizing the gain through each of the MZI's two waveguide paths. While the filters are normalized in passband amplitude, the filter frequency was re-normalized in real-time using on-chip PMs. (b) Showing tunability in frequency across a full FSR. The parasitic loss of the phase modulators is demonstrated in this measurement as an increase in the extinction of the zero filter as the loss equalizes the optical amplitude in the two waveguides of the MZI.

To ensure that only a single sideband of the LO was down-converted, the reflection spectrum of a fiber Bragg grating (FBG) was utilized. This band-limited reflection spectrum was 0.3 nm (37.2 GHz) wide and had 30 dB out of band extinction, and so the output of the filter illuminated only the upper sideband of the LO. The resultant optical signal was

impinged upon a high-speed photodetector and the electrical spectrum viewed on a 50 GHz ESA. All measurements were made continuous-wave and at room temperature, with constant device temperature maintained with a thermoelectrically cooled stage. The device was wire bonded onto a Al_2O_3 carrier and light was coupled in and out via lensed fiber.

4.2 Measured filters

Single unit cells were fabricated and evaluated. Measured 3rd order coupled-ring bandpass filters are shown in Fig. 7 together with theoretical fits and accompanying pole-zero plots. These Chebyshev Type I approximations have bandwidths of 7.06, 5.50, and 3.90 GHz, set by inter-ring power coupling values of 25.5%, 15.6%, and 8.41%. Extinction increases with decreased inter-ring coupling, and up to ~40 dB was measured here. In order to synthesize the 3.90 GHz filter, the 400 μm long SOAs were biased at 16.5 mA, giving a gain of about 1.3 dB to achieve the desired intrinsic pole values of 0.65 for the outer rings and 0.84 for the center ring. At this setting, the chip consumed approximately 200 mW. The 1.3 dB gain is significantly lower than the 10 dB max gain available in the fabricated SOAs, indicating room for optimization of material and device design. The electrical spectrum of the 3rd order filters are normalized in amplitude for clarity. However, there is zero optical insertion loss through the chip as the coupling and waveguide losses are negated by the on-chip amplifiers. In this measurement, input and output SOAs placed before and after the 3 coupled rings were used to account for the coupling losses. It is possible to eliminate the input and output amplifiers (and hence their added noise) and instead tune the desired system gain by biasing the intra-ring SOAs accordingly. For example, in Eq. (4) the 2nd order coupled-ring response gain can be increased without changing the filter shape by increasing A_2 and decreasing A_1 such that A_1A_2 remains the same. The results are also normalized in frequency, but are tunable across a full FSR, indicating the ability to place a filter anywhere in the c-band.

Figure 8 displays 2nd order coupled-ring bandpass filters showing such tunability across 30 GHz. Filters are tuned by adjusting the phase modulators in both rings and compensating for the resulting parasitic loss by re-tuning the SOAs to obtain a flat topped filter. Tunability of the 1st order zero is also shown via an all-optical measurement in Fig. 9, utilizing a broadband ASE input and an optical spectrum analyzer (OSA). The parasitic loss of the phase modulators is demonstrated in this measurement as an increase in extinction as the loss equalizes the optical amplitude in the two waveguides of the MZI. In practice, the zero filter extinction can be tuned from 0 dB to its maximum value of about 20 dB by adjusting the SOA gain in each MZI arm.

5. Conclusion

Coupled-ring optical filters are a promising solution for telecom and RF filtering applications. Here we have described the z-transform representation of 2nd and 3rd order filters. A 3rd order coupled-ring filter was monolithically integrated in the InP/InGaAsP material system and new measured filter results were shown along with theoretical fits demonstrating tunability in bandwidth and frequency. Future work will explore the effects of ASE noise and RF distortion on the dynamic range of a microwave photonic system employing such an active filter. Other areas of further study include active control systems to ensure filter stability with regards to temperature fluctuations. For applications that require near-ideal filter approximations with high extinction, fast roll-off, and a flat passband, active solutions provide benefits over all-passive approaches.

Acknowledgments